

AUTOMATIC OFF-RESONANCE AND CONCOMITANT GRADIENT CORRECTION IN SPIRAL MRI

A Thesis

Presented to
the faculty of the School of Engineering and Applied Science
University of Virginia

in partial fulfillment
of the requirements for the degree

Master of Science

by

Matthew Restivo

August

2012

APPROVAL SHEET

The thesis
is submitted in partial fulfillment of the requirements
for the degree of
Master of Science

Matthew Restivo
AUTHOR

The thesis has been read and approved by the examining committee:

Craig H. Meyer
Advisor

Freddie H. Galt

[Signature]

Accepted for the School of Engineering and Applied Science:

James H. Ayler

Dean, School of Engineering and Applied Science

August

2012

Abstract

Spiral magnetic resonance imaging (MRI) has many desirable qualities over 2DFT imaging, such as speed and suppression of motion artifacts. A major limitation of spiral imaging is that it is very sensitive to off-resonance effects that result in image blurring. We can correct for these effects given accurate field maps of the off-resonant frequencies and concomitant field magnitudes in a process termed deblurring. The off-resonance map is not known prior to scanning but can be calculated either during the scan or during image reconstruction. The most intuitive way is to collect two single shot images prior to collecting the data and infer the off-resonance from the phase accrual.

Often situations arise where using extra scan time to acquire a field map is undesirable. In that case, we desire to use a reconstruction method that does not require an acquired field map. Such reconstructions that do not require field maps are referred to as “automatic”. Automatic deblurring on its own is known to often be prone to errors. To account for this, we propose a method that does automatic deblurring in two stages in order to suppress field map estimation errors. Additionally, we improve on previous automatic methods by using optimized parameters and implementing a better field map approximation using robust regression.

Through simulating image reconstructions, we show that this method is successful in correcting blurry images. We use phantom images so that we can easily access blurring and compare our method to other deblurring methods. We prove the robustness and validity of each method by using image data from various inhomogeneity profiles and imaging parameters.

We conclude that our method is as effective as previous non-automatic methods with the additional benefit of reducing scan time. The method we created is an optimized automatic off-resonance and concomitant gradient correction algorithm which can be used in place of field map based correction. We have shown the validity of this method both on phantom reconstructions and in-vivo with very positive results. A non-automatic method is still preferred when we can acquire a field map with no penalty due to its robustness and computational efficiency.

Table of Contents

Chapter 1: Introduction	1
Spiral Imaging.....	1
Off-Resonance and Concomitant Gradients	2
Deblurring	4
Objective	4
Chapter 2: Background	6
Field Map Generation	6
Acquiring a Field Map	6
Automatic Field Map Generation	7
Discussion of Spurious Minima	9
Linear Correction	12
Conjugate Phase Reconstruction and Fast Approximations	13
Semiautomatic Correction	16
Chapter 3: Two-Stage Automatic Correction.....	19
Introduction	19
Clinical Importance	21
Method	22
First Stage Parameters	24
First Stage Readout Time	24
Summation Window Size	27

Polynomial Fitting and Robust Regression	29
Algorithm	32
Code	33
Chapter 4: Results	36
Acquiring Data and Images	36
Phantom Results	37
In-Vivo Results.....	41
Computational Efficiency	46
Chapter 5: Discussion and Conclusion	47
Discussion.....	47
Recommendations for Future Work	47
Conclusion.....	49
Chapter 6: Bibliography	50

Table of Figures

Figure 2.1: An automatic field map calculated from a full resolution phantom image	Error! Bookmark not defined.
Figure 3.1: Spiral pulse sequence used in field map based off-resonance correction algorithms	21
Figure 3.2: Map of 4 spiral interleaves in k-space.	Error! Bookmark not defined.
Figure 3.3: Comparisan of first stage readout times	27
Figure 3.4: Comparisan of summation window sizes	29
Figure 3.5: Comparison of different IRWLS weighting functions	31
Figure 3.5: Comparison of polynomial fits to the given field map	32
Figure 3.6: Polynomial IRWLS fit using a talwar weighting function	32
Figure 4.1: Axial slice with a well shimmed field at isocenter	37
Figure 4.2: Axial slice with an added linear shim gradient	39
Figure 4.3: Axial slice with a 90 mm offset in Z	40
Figure 4.4: Water/Fat Phantom.	41
Figure 4.5: Result of correction methods on in-vivo data	42
Figure 4.6: Another in-vivo spiral perfusion reconstruction	42
Figure 4.7: SSIM of the automatic correction method compared to the semiautomatic method	43
Figure 4.8: RMSE of the automatic correction method compared to the semiautomatic method	44
Figure 4.9: Comparisan of deblurring on a coronary artery image	45

Chapter 1

Introduction

Magnetic resonance imaging (MRI), although typically used for imaging anatomy, is also an important tool for non-invasive assessment of physiological function. When imaging physiological processes that occur over time, additional consideration must be given to specifications such as motion sensitivity and temporal resolution. In these situations, it is often desirable to acquire images in very short periods of time. Therefore, fast imaging methods, such as spiral imaging, are typically used for such dynamic imaging applications.

Spiral Imaging

In MRI, images are sampled from the MR signal in the two-dimensional Fourier transform domain, called k-space. Traditionally, k-space is sampled on a Cartesian grid, with each line of k-space collected separately, and this is called 2DFT imaging. In spiral imaging, k-space is sampled in a spiral trajectory (1). A spiral can cover all of k-space in a single shot, therefore drastically reducing the number of excitations and readouts used to acquire a single image. In practice, we use interleaved spiral readouts to cover k-space. One reason for this is that interleaving causes the SNR to increase by \sqrt{N} versus a single shot image, where N is the number of excitations and interleaves. Spiral interleaving also allows for higher spatial resolution

at a given readout length (1). The number of readouts necessary in spiral imaging is still significantly fewer than in Cartesian imaging and thus it is significantly faster.

The advantage to spiral sequences in dynamic imaging is that spiral sequences are less sensitive to motion and flow artifacts (1,2). This is particularly beneficial when imaging things such as the heart or blood vessels because they are most commonly subjected to artifacts due to motion and flow.

The disadvantage of spiral imaging is that spiral images are much more sensitive to sources of off-resonance than 2DFT imaging. Off-resonance is caused by inhomogeneity in the magnetic field that is generally unavoidable. While off-resonance in 2DFT images is tolerable and only results in geometric distortion, off-resonance in spiral images results in destructive blurring (2).

Off-Resonance and Concomitant Gradients

MR image reconstruction usually assumes that all the spins in the object are precessing on-resonance, with the resonant frequency being determined by the main magnetic field strength and any applied gradients. However, in reality, the main magnetic field is inhomogeneous and the actual rate at which the spins are precessing is proportional to the local magnetic field strength. When spins are precessing at different rates than the expected resonant frequency due to variations in the main magnetic field, we call them off-resonant. Chemical shift is a known source of off resonance that occurs when the object contains chemical species whose protons precess at a different frequency than water. For example, fat has a chemical shift relative to water of 3.5 ppm, or 445 Hz at 3 T. Chemical shift off-resonance can be mitigated by applying spectrally selective RF pulses to only excite water or apply fat saturation pulses to suppress

signal from fat. Off-resonance also occurs at magnetic susceptibility interfaces. For example, tissue and air have different magnetic susceptibilities, which causes local distortion in the magnetic field at those interfaces. Before imaging the magnet is shimmed to try to correct for inhomogeneities, but shimming only corrects for low order variations in the magnetic field and cannot correct for higher order field variations.

All of the sources of off-resonance listed above will vary the frequency of precession of the magnetic dipoles resulting in time dependent phase shifts in the object. It is this extra phase accrual that results in blurring in non-2DFT images upon image reconstruction.

Concomitant gradients also cause unwanted phase in the image that will lead to blurring. The concomitant magnetic field is a side effect of implementing linear field gradients. From Maxwell's equations, it is known that any uniform imaging gradient will be accompanied by higher order spatially varying magnetic fields (3). Solving for the concomitant field gives the following equation for concomitant field strength as a function of position:

$$B_c = \left(\frac{g_z^2}{8B_0} \right) (x^2 + y^2) + \left(\frac{g_x^2 + g_y^2}{2B_0} \right) z^2 - \left(\frac{g_x g_y}{2B_0} \right) xz - \left(\frac{g_y g_z}{2B_0} \right) yz \quad (1.1)$$

Where x, y, and z are spatial coordinates; g_x , g_y , and g_z are time varying field gradients; and B_0 is the main magnetic field strength. Concomitant phase is slightly more complicated than off-resonant phase because it is not directly proportional to time. Instead, concomitant phase φ_c is given by

$$\varphi_c = \gamma \int_{-\infty}^t B_c dt' \quad (1.2)$$

Since imaging gradients are on every time data is read out, concomitant phase will always affect MR data, except for special cases related to the orientation of the slice being imaged.

Deblurring

The effects of blurring can be corrected for given accurate maps of the off-resonant frequencies and concomitant field magnitudes in a process termed deblurring (2). Knowledge of the concomitant field map is given from the solution to Maxwell's equations and can be calculated from the slice orientation, gradient waveforms, and the main magnetic field strength (3). The off-resonance map is not known prior to scanning but can be calculated in two ways. The first is to collect two single shot images prior to collecting the data and infer the off-resonance from the phase accrual (4). The second method calculates an off-resonance map from the image itself and does not require extra scan time (2). This technique is referred to as "automatic" deblurring because it does not require a known field map or any input from the user to correct for off-resonance. A previous technique developed by Chen, et, al. combines both off-resonance field map calculation strategies, where a low resolution field map is acquired in the first stage and is used as a constraint for a second stage using automatic deblurring (5). This "semiautomatic" method has been shown to be more successful in deblurring than previous correction techniques. It is also advantageous because it is computationally efficient when implemented using the Chebyshev approximation to conjugate phase reconstruction and also can easily be made to correct for concomitant field effects as well (6).

Objective

Often situations arise where using extra scan time to acquire a field map is undesirable. In that case, we desire to use a fully automatic deblurring reconstruction. Automatic deblurring on its own is known to suffer from inaccuracies, particularly related to *spurious minima* (7). To account for this, we propose a method that does automatic deblurring in two stages similar to the

semiautomatic method, but without acquiring a field map. The first stage computes a low resolution approximation to the real map, and then we use that map as a constraint for a second stage automatic map calculation. Multi-stage automatic methods have been proposed before by (7-8); however, these methods are not computationally efficient. Additionally, we improve on these previous methods by using optimized parameters and implementing a better approximation to the field map using robust regression. We then evaluate our new method through both phantom and in-vivo simulated reconstructions and compare the results to the current gold standard correction method.

Chapter 2

Background

This chapter is a review of existing methods used to correct non-2DFT images. The process of deblurring involves calculating a map of the off resonance, termed field map, then using that map is to reconstruct a corrected image. In this chapter, typical approaches to field map generation will be discussed first. Following that is a discussion on reconstruction methods given knowledge of the field map. The chapter culminates in a summary of a technique termed “semiautomatic” correction which uses many of the techniques outlined in the chapter and is the current gold standard deblurring algorithm used in our lab.

Field Map Generation

Correction for off-resonance in images requires knowledge of what off-resonance is present in the image. A field map is a spatial image that tells us what the effective magnetic field is in that particular portion of the image. Because frequency is proportional to the magnetic field strength by the gyro-magnetic ratio, the field map is usually given as the difference in hertz between the expected resonant frequency and the actual resonant frequency of spins in the object.

Acquiring a Field Map

An approximation of the field map can be easily found by examining phase accrual over time. To do this, we collect two single shot spirals spaced one millisecond apart. We can then determine the off-resonant frequency by calculating the phase angle that has accrued from the first image to the second image and dividing by the time between acquisitions (4). This process can be seen mathematically through the following equations.

$$I_1(x, y) = \rho_1(x, y)e^{-i2\pi(TE_1\Delta f(x, y))} \quad (2.1)$$

$$I_2(x, y) = \rho_2(x, y)e^{-i2\pi(TE_2\Delta f(x, y))} \quad (2.2)$$

I_1 and I_2 are the images acquired at echo times TE_1 and TE_2 respectively. Given that the difference in echo time between I_1 to I_2 is known, we can solve for the off-resonance map using equations 2.3 and 2.4.

$$I_1^* I_2 = \rho_1 \rho_2 e^{-i2\pi(\Delta f(x, y)(TE_2 - TE_1))} \quad (2.3)$$

$$\Delta f(x, y) = \frac{\text{angle}(I_1^* I_2)}{2\pi(TE_2 - TE_1)} = \frac{\text{angle}(I_1^* I_2)}{2\pi\Delta t} \quad (2.4)$$

Equations 2.1 and 2.2 assume that the image phase is only a function of off-resonance. While this is not completely true, most other sources of phase accrual will be the same in both images and will cancel out in equation 2.3, where the phase of the product of I_1^* and I_2 is the difference of the phase of each individual image. Concomitant phase will also be the same in both images assuming the same readout gradient is used.

Automatic Field Map Generation

The basic technique for automatic field map calculation is to demodulate the raw data by a range of frequencies and reconstruct a series of base images. The blurring in these base images

is then quantified using an objective function. An off-resonant frequency map is then assembled by determining which demodulation frequency minimizes blurring at each pixel in the image (2).

In our implementation, we choose our objective function to be the absolute value of the imaginary component of the image. The rationale behind this is that the point spread function of an impulse reconstructed at the resonant frequency is all real (5). Since we assume that phase due to off-resonance accrues linearly as a function of time, using this objective function requires that there be no phase present in the image at time zero. In practice, there is always incidental phase caused by the RF pulse and other effects; therefore, we must subtract out this phase before evaluating the objective function. To do this, we reconstruct an additional image for each of the demodulated images that only uses the first 1.6 milliseconds of the acquired signal. It is reasonable to assume that little of the phase accrual in that time has been due to off-resonance and that the phase is mostly incidental. Below is a more detailed mathematical explanation of automatic reconstruction.

The signal equation including B0 field inhomogeneity, concomitant gradient field, and incidental phase, and ignoring relaxation, is shown below:

$$s(t) = \int_{-\infty}^{\infty} m(r) \exp(-j2\pi k(t) \cdot r - j\varphi(\Delta\omega(r), \Delta\omega_c(r), t) - j\varphi_{ip}(r)) dr \quad (2.5)$$

The term $\varphi(\Delta\omega(r), \Delta\omega_c(r), t)$ represents the phase accrual due to both B0 field inhomogeneity ($\Delta\omega(r)$) and the concomitant field ($\Delta\omega_c(r)$). The term $\varphi_{ip}(r)$ represents the incidental image phase present at time zero. A series of images can be reconstructed at frequency bins $\Delta\omega_i$ using conjugate phase reconstruction as shown in equation 2.6.

$$m(r; \Delta\omega_i) = \int_0^T s(t) W(t) \exp(j2\pi k(t) \cdot r + j\varphi(\Delta\omega_i(r), \Delta\omega_c(r), t)) dt \quad (2.6)$$

$W(t)$ is the density compensation function necessary to correct for the density variation in sampled k-space due to spiral trajectories (12). The upper-bound on the time integral, t_{ip} , is typically the entire readout time. However, it is often beneficial to limit t_{ip} in the first stage reconstruction to reduce spurious minima, which will be discussed in the next section. The concomitant phase term is a function of the slice position and gradient waveform. Since it is image independent, the concomitant map, $\Delta\omega_c(r)$, can be calculated prior to demodulation.

It is also necessary to reconstruct incidental phase images at each demodulation frequency in order to subtract out incidental phase when calculating the cost function. This is shown in the following two equations 2.7 and 2.8.

$$m_{ip}(r; \Delta\omega_i) = \int_0^{t_{ip}} s(t)W(t) \exp(j2\pi k(t) \cdot r + j\varphi(\Delta\omega_i(r), \Delta\omega_c(r), t)) dt \quad (2.7)$$

$$\epsilon(r; \Delta\omega_i) = \int_{H(r)} |im\{m(r; \Delta\omega_i) \cdot \exp(j \cdot angle(m_{ip}(r; \Delta\omega_i))\}|^\alpha dr \quad (2.8)$$

The integral in equation 2.8 represents a summation window, $H(r)$, around the pixel of interest used to calculate a more robust value of the cost function. The power, α , is a constant that allows for tuning of the objective function. The typical value of α can range from .5 to 1.

Finally, the map is calculated by determining the frequency that minimizes the cost function for each pixel.

$$map(r) = arg \min_i \{\epsilon(r; \Delta\omega_i)\} \quad (2.9)$$

Discussion of Spurious Minima

The problem limiting effectiveness of the automatic method is that it is often sensitive to artifacts termed spurious minima. A spurious minimum is an error in the field map caused by the objective function being minimized by the incorrect off-resonant frequency. This occurs in two scenarios: in parts of the image that contain no signal and in parts of the image where the

absolute phase accrual is greater than one cycle. In the case of parts of the image containing little or no signal, the phase of the image is determined by random noise, leading to noise in the field map. When image phase accrual is more than one cycle, there are multiple frequencies that can minimize the objective function leading to the wrong frequency often being chosen for the map. Figure 2.1 is an example of an automatically calculated field map that contains numerous spurious minima.

Because we know the cause of spurious minima, there have been techniques proposed for avoiding them in automatic field map generation. One proposed technique is to reconstruct the base images using only the center portion of k-space. The low frequency k-space data is acquired first in our spiral sequence and thus image phase has less time to accrue. Another technique is to increase the size of the summation window in the objective function. Summing over a larger number of neighboring pixels leads to a smoother field map that is less tolerant of spurious minima due to noise, helping to solve the problem of regions of the image containing little or no signal (7-8). Implementing these two techniques helps suppress spurious minima but also results in a field map lacking spatial resolution.

It is also possible for an acquired field map to exhibit spurious minima due to the phase accrual of more than one cycle during the time between spirals. However, this is rare and only possible in the presence of very large off-resonant frequencies.

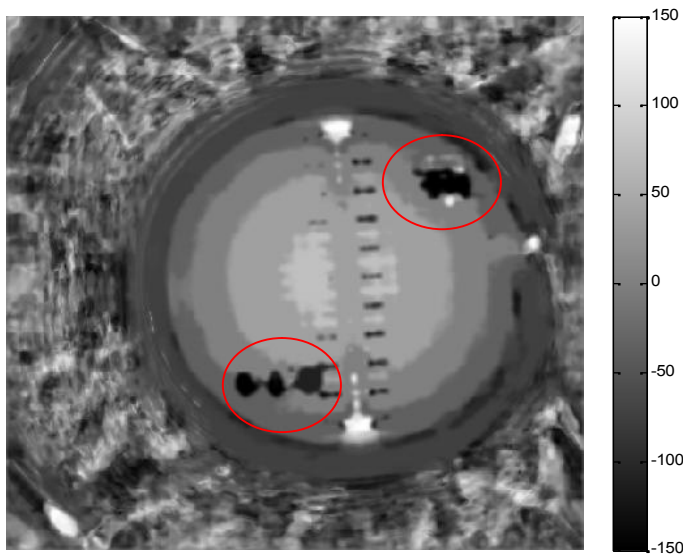


Figure 2.1: An automatic field map calculated from a full resolution phantom image. The spurious minima are characterized by the spots of the image that appear to not fit the general trend of the map. The scale on the right is in Hz. Spurious minima manifest in this map because the readout length for each spiral was sufficiently long to allow for more than a cycle of phase to accrue in the base images. All the points outside of the area of the phantom can also be considered spurious because they do not accurately represent the actual off-resonant frequencies present in that part of the image

Another technique to avoid spurious minima is to constrain the range of frequency demodulation. The frequency at which a spurious minimum occurs has to deviate significantly from the real resonant frequency such that at least one cycle of phase accrues. Thus, the likelihood of encountering spurious minima, in the case of automatic field map generation, is significantly reduced when we limit the range of frequencies that we search over to be sufficiently small. This is the theory behind both semiautomatic and two-stage automatic off-resonance correction (5). Both these methods use two stages of field map generation to first

estimate the low resolution field map and then use a constrained frequency search to calculate a final, more accurate field map from which the de-blurred image is reconstructed.

Linear Correction

The most computationally efficient and straightforward approach to off-resonance correction is to only correct for the linear off-resonance terms (10). If the off-resonance is a linear function of position (as shown in Eq. 2.10), then the signal equation can be written as shown in Eq 2.11.

$$\omega = \omega_0 + \omega_x x + \omega_y y \quad (2.10)$$

$$S(t) = e^{i2\pi\omega_0 t} \int M(x,y) e^{j2\pi[(k_x + \Delta k_x)x + (k_y + \Delta k_y)y]} dx dy \quad (2.11)$$

In Eq. 2.10, ω_0 , ω_x and ω_y are constants that describe linear off-resonance with units of Hertz per centimeter. In Eq. 2.11, k_x and k_y are linear functions of time as described below.

$$\begin{aligned} k_x(t) &= \omega_x t \\ k_y(t) &= \omega_y t \end{aligned} \quad (2.12)$$

Linear correction has almost no computational time penalty. As can be seen in Eq 2.11, the phase accumulation can be removed by simply demodulating by the center frequency ω_0 and then shifting the k-space locations by k_x and Δk_y during gridding.

The parameters of linear correction (ω_0 , ω_x and ω_y) are obtained from applying a linear least-squares fit to the calculated field map. The other benefit of linear correction is that a completely accurate field map is unnecessary because it only determines the center frequency and linear components. It has been shown that even a standard automatic field map is generally sufficient for linear correction (11).

Conjugate Phase Reconstruction and Fast Approximations

Linear correction only corrects for linear off-resonance terms and therefore it does not fully correct the image when there are higher order inhomogeneities. Assuming that the off-resonance field map is known, we can correct the image using conjugate phase (CP) reconstruction (12). CP reconstruction assumes that if the signal exhibits unwanted time varying phase due to off-resonance, we can subtract out the phase by multiplying the signal by a term with a phase of the opposite sign. We know that the signal equation of an MR image considering only off-resonance and ignoring relaxation is the following:

$$S(t) = \int_{\text{voxel}} m(r) e^{-j(2\pi k(t)r + \Delta\omega(r)t)} dr \quad (2.13)$$

Where $S(t)$ is the signal received from the object and $m(r)$ is the image in the spatial dimension. The term $\omega(r)$ represents spatially varying off-resonance. We can easily see through the signal equation how off-resonance adds linear phase to the signal. Therefore, to reconstruct the image we need to multiply by the conjugate phase.

$$m(r) = \int_0^T S(t) W(t) e^{j(2\pi k(t)r + \Delta\omega(r)t)} dt \quad (2.14)$$

Where $e^{j\Delta\omega t}$ is the conjugate phase term and $W(t)$ is the density compensation function necessary to correct for the density variation in sampled k-space due to spiral trajectories (12). It can be seen in the above equation that off-resonance is a function of position but the integral is evaluated in the time domain. This means that we must reconstruct each pixel independently according to its unique off-resonance frequency given by $\omega(r)$. CP reconstruction can therefore be very slow when the off-resonance profile is not uniform across the image. In practice, to evaluate the CP integral for spirals we grid the modulated k-space data onto the Cartesian grid

and reconstruct the image using an inverse FFT. This means that a computationally intensive gridding operation must be performed when reconstructing each pixel in the image. Obviously this is very slow and undesirable. Fortunately, there are a number of fast approximations to CP reconstruction that drastically decrease necessary computation.

The simplest approximation to CP reconstruction is to demodulate the image at a range of equally spaced frequency bins $\Delta\omega_i$, like we already do in automatic correction.

$$m(r, \Delta\omega_i) = \int S(t) e^{j\Delta\omega_i t} W(t) e^{j2\pi k(t)r} dt \quad (2.15)$$

We can then pick the image value for each pixel based from the bin image that was demodulated at the frequency nearest to that of each pixel's known off-resonant frequency (13). This method saves a lot of computational time because it only requires that a reasonable number of reconstructions to be performed versus reconstructing an entire image for each pixel.

A better method to approximate CP reconstruction is Multi-frequency Interpolation (MFI) (13). MFI comes closer to approximating ideal CP reconstruction by using the assumption that the real conjugate phase can be represented as a weighted sum of the conjugate phase terms evaluated at the different bin frequencies.

$$e^{j\Delta\omega t} \approx \sum_{i=0}^L C_i(\Delta\omega) e^{j\Delta\omega_i t} \quad (2.16)$$

In the above equation, $C_i(\Delta\omega)$ represents a series of coefficients for the off-resonance term that when multiplied by the corresponding phase term, $e^{j\Delta\omega_i t}$, sum to approximate the actual conjugate phase at $\Delta\omega$. The constant L is the number of frequency bins used and thus the number of coefficients needed. These MFI coefficients can be pulled out of the integral, resulting in the equation:

$$m(r) \approx \sum_{i=0}^L C_i(\Delta\omega(r)) S(t) e^{j\Delta\omega_i t} W(t) e^{j2\pi k(t)r} dt \approx \sum_{i=0}^L C_i(\Delta\omega(r)) m(r; \Delta\omega_i) \quad (2.17)$$

This allows us to approximate the solution to the actual CP reconstruction while only reconstructing L images, the same number used in segmented CP reconstruction. Solving for the coefficients C_i can be done by finding the least squares solution to equation 4 as shown in (13).

An even more efficient way to approximate the conjugate phase term was proposed by Chen involving using the Chebyshev function approximation method. This method involves solving for the coefficients of the Chebyshev polynomials that when summed is approximately equal to the desired function (6).

The definition of a Chebyshev approximation is shown below where $f(t)$ is the function being approximated, C_k is the coefficient corresponding to the k^{th} Chebyshev function, T_k (14).

$$f(t) \approx \left[\sum_{k=0}^{N-1} C_k T_k(t) \right] - \frac{1}{2} C_0 \quad (2.18)$$

Chebyshev functions are defined iteratively over the interval $t = [-1, 1]$, where

$$\begin{aligned} T_0(t) &= 1 \\ T_1(t) &= t \\ T_{n+1}(t) &= 2t \cdot T_n(t) - T_{n-1}(t) \end{aligned} \quad (2.19)$$

It is known that off-resonance phase varies linearly with time and concomitant gradient phase varies as a function of the gradient waveform as shown below.

$$\varphi(\Delta\omega(r), t) = \omega(r)t \quad (2.20)$$

$$\varphi_c(\omega_c(r), t) = \omega_c(r)T_c(t); \text{ Where } T_c(t) = \frac{1}{g_{\text{r}}^2} \int_0^t g_0^2(t') dt' \quad (2.21)$$

In Eq 2.21, g_0 and g_m are the amplitude of the readout gradient as a function of time and the maximum readout gradient amplitude, respectively. Given that the readout gradient is known, the conjugate phase term as a function of off-resonance, concomitant field, and time is simply:

$$f(\Delta\omega, \Delta\omega_c, t) = e^{i\Delta\omega t + i\Delta\omega_c T_c(t)} \quad (2.22)$$

Using Eq. 2.18, this term can be approximated by solving for the corresponding Chebyshev coefficients with the given off-resonance and concomitant field. To save time computationally, the Chebyshev coefficients over the entire range of possible ω and $\Delta\omega_c$ values are solved for offline and compiled in a table. Thus, the conjugate phase term for any combination of off-resonance, concomitant field, and readout time can be approximated using the following equation.

$$f(t) \approx \left[\sum_{k=0}^{N-1} C_k(\Delta\omega, \Delta\omega_c, \tau) T_k(t) \right] - \frac{1}{2} C_0(\Delta\omega, \Delta\omega_c, \tau) \quad (2.23)$$

Two key benefits come out of using the Chebyshev polynomial approximation. First, the gridding operation only needs to be performed once per CP reconstruction. Second, we can include concomitant phase in the function approximation making the Chebyshev coefficients a function of both off-resonance and concomitant phase (6). Therefore we can combine the off-resonant map and the concomitant map to find the coefficients $C_i(\Delta\omega, \Delta\omega_c, \tau)$ such that the conjugate phase term will correct for both sources of blurring.

Semiautomatic Correction

Semiautomatic off-resonance correction generates a field map in two stages. A first stage low resolution acquired field map serves as a base for a frequency constrained automatic off-resonance field map. Each pixel in the subsequent image bins is reconstructed at frequency shifts

relative to the acquired map (5). For example, if the acquired map estimates an off-resonant frequency of 60 Hz for a particular pixel, then our reconstructed base images would shift the pixel through a small range of frequencies around the predicted frequency of 60 Hz.

Due to the fact that we constrain the frequency search in the second stage, we do not encounter spurious minima in the automatic field map. Other steps to avoid spurious minima do not need to be taken, therefore allowing us to reconstruct high resolution base images and generate a high resolution map.

Semiautomatic off-resonance correction is more computationally intensive than traditional field map based correction due to the addition of an automatic stage. However, traditional field map based correction is inadequate because an acquired field map is not sufficient to completely deblur an image. Acquired field maps can be inaccurate due to the fact that phase difference is not exactly proportional to the echo time in the presence of off-resonance (5). Acquired field maps are also sensitive to noise. Multishot spirals would increase SNR, but that would prolong scan time. Using a constrained frequency search automatic stage helps correct the acquired field map without inciting additional errors due to the unreliability of the automatic correction method.

Chen proposes two strategies to perform semiautomatic correction. The first is the computationally efficient strategy that performs linear correction before the automatic stage. Then automatic reconstruction only searches for the higher order off-resonance terms. The second strategy is to fit the map using a higher order polynomial weighted least squares approximation. The weight in this method comes from the magnitude image acquired from one of the single shot spiral. This is a much more robust technique for correcting images with strong

non-linear components. The result of that study is that the high order polynomial approximation worked better than the linear semiautomatic reconstruction due to the fact that susceptibility can cause sudden field variations that are highly non-linear (5).

Results from this method have been very successful. In (5), Chen shows that semiautomatic deblurs both phantom and in-vivo data better than correction using high resolution field map and linear correction. With the incorporation of Chebyshev polynomials to give fast approximations to CP reconstruction and the ability to correct for concomitant gradients, this method has proved to be very computationally efficient.

Semiautomatic correction will serve as the starting point for our proposed improved two stage automatic method. It will also be a good reference to which we can compare our results. Examples of semiautomatic reconstructions can be found in Chapter 4 where we show results for both semiautomatic and our proposed two-stage automatic method.

Chapter 3

Two-Stage Automatic Correction

Introduction

As discussed in Chapter 1, often situations arise where an MRI scan will be time limited. Cardiac imaging sequences will almost always be time limited because we often want to scan during the relatively quiescent period between heartbeats to avoid severe motion artifacts. Due to this, it is important that we use scan time efficiently, either to acquire as many slices as possible or improve image quality through better SNR or resolution. In the case of field map based correction, including semiautomatic correction, at least two extra spirals need to be collected before every slice to determine an off-resonance map. However, as discussed the previous chapter, it has been shown by (2,15) that a field map can be estimated from the image data alone, using the automatic method, thus making it unnecessary to use extra scan time to acquire a field map. Figure 3.1 (16) highlights the field map acquisition portion of the spiral perfusion pulse sequence. Skipping field map acquisition will allow for more time to be allocated to the other parts of the sequence without a loss of image quality. That time can be used to either collect additional slices, collect more interleaves, or increase the flip angle of the RF pulse.

Traditionally, the automatic method is not favorable for field map generation due to errors that are intrinsic to this technique, particularly spurious minima. The goal of the proposed

method is to modify the automatic field map generation and correction algorithm to make it less susceptible to artifacts. Ideally, it should be able to deblur spiral images with effectiveness similar to that of the semiautomatic method. To do this we propose a two-stage method that is fully automatic. Two stage automatic methods have been proposed previously (7,8). However, these methods are computationally inefficient and still tend to be prone to the inaccuracies attributed the automatic field map estimation. They also do not include any of the recent advances in the field of spiral correction such as Chebyshev CP approximation and concomitant gradient correction. We hope to show that with the addition of techniques learned from semiautomatic correction, as well as some new techniques for choosing parameters and field map estimation, we can drastically improve on previous two stage automatic reconstructions.

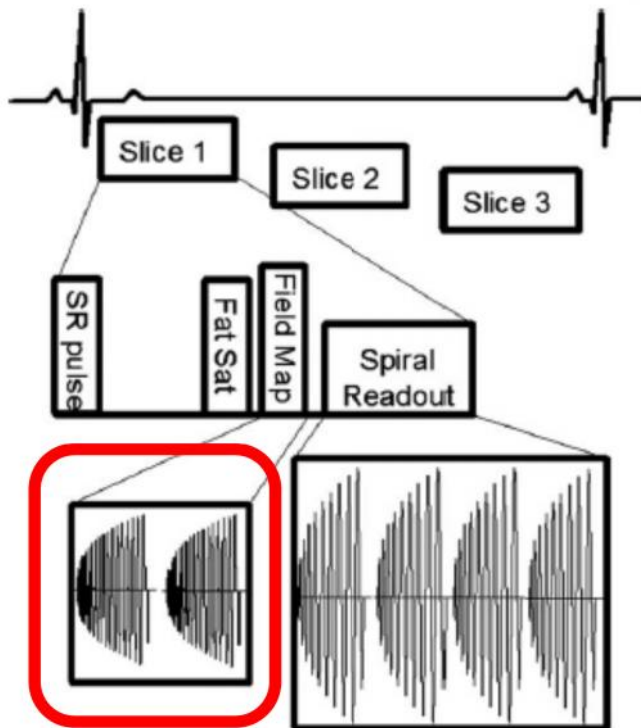


Figure 3.1: Spiral pulse sequence used in field map based off-resonance correction algorithms (16). Highlighted in red is the portion of the sequence associated with field map acquisition. We desire to remove the highlighted portion allowing more time to be allocated to acquiring more useful information.

Clinical Importance

One motivation behind my research is to advance the current state of myocardial stress perfusion imaging. An example of this is shown in the in-vivo results (Fig. 4.5). Stress perfusion imaging is a powerful non-invasive tool for evaluating the presence and severity of coronary artery coronary artery disease (CAD). CAD occurs when the small blood vessels that supply the heart with blood become narrowed. This causes the heart to become ischemic, which is noticeable in the time course profile of the tissue perfusion. Ischemia is especially noticeable during exercise when heart perfusion should be heightened. For that reason, stress perfusion imaging is the best way to observe and quantify CAD. During a first pass stress perfusion CMR, a time course of images is taken of the ventricles as a bolus injection of contrast agent passes

through the heart. A doctor can diagnose CAD by determining the perfusion abnormalities in these images. Compared to similar tools to observe CAD, like SPECT, MRI has the advantage of being higher resolution and does not subject patients to any radiation. Being able to accurately diagnose and quantify CAD is very important due to the fact that it is the leading cause of death for both men and women in the United States.

Using automatic deblurring in spiral myocardial perfusion imaging, we can use the extra time to collect more slices or increase the quality of the slices already acquired. Imaging an additional slice per heartbeat could be beneficial clinically because it allows us to see more of the heart. Collecting more interleaves or increasing the flip angle would improve the SNR.

Method

Techniques to avoid spurious minima were briefly described in Chapter 2. In summary, we can adjust the parameters of the automatic field map generation algorithm to reduce the likelihood of calculating spurious points. Those parameters include the readout length (shown in

Fig. 3.2), the summation window size, and the frequency search range.

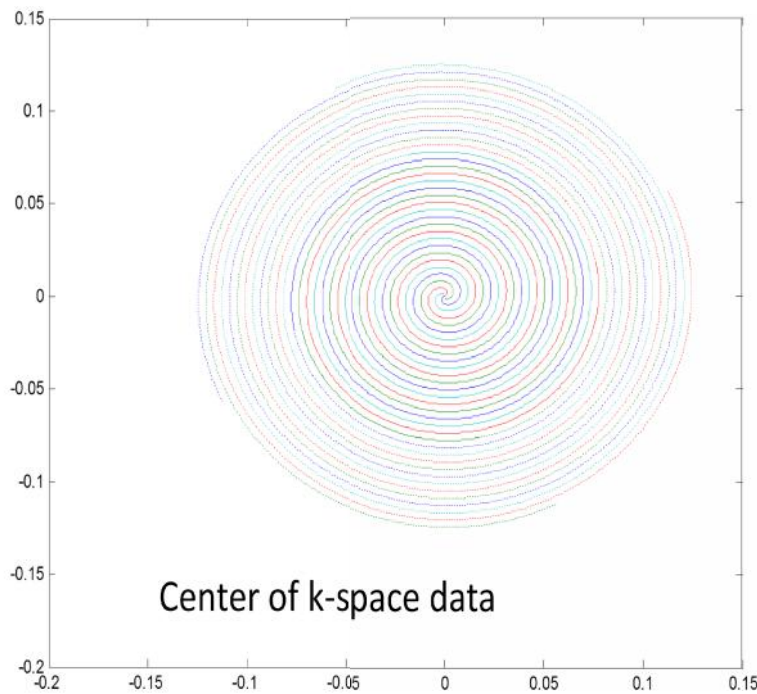


Figure 3.2: Map of 4 spiral interleaves in k-space. The dark lines indicate the part of the readout that we want to use for our first stage map in fully automatic correction and the dashed lines indicate the part of the readout we ignore. We only use the initial segment of the readout so that we can avoid large phase accrual (± 1 cycle) in the reconstructed images.

It is clear that applying these techniques all at once would not result in adequate image correction. Using only the center of k-space data does not use the full acquired resolution of the images. A large summation window reduces the spatial resolution of the field map that is used for correction. Additionally, the correction method should be robust enough to correct for the full range of possible off-resonant frequency values. However, using multiple stages allows these techniques to be implemented in a way that they become beneficial. In a two stage automatic method, an automatic first stage is modified to give an approximation to the field map that is

generally void of spurious minima. Then the automatic second stage uses a constrained search to more accurately choose the correct off resonant frequency.

The strength of this proposed two stage automatic method is that we improved the algorithm to **a) optimally reduce spurious minima in the first stage by choosing the best parameter values** and **b) implement a better, more robust, scheme to fit the estimated first stage map before second stage correction.**

First Stage Parameters

Choosing the right parameters for this program is very important. It is necessary to adequately suppress spurious minima in order to generate a sufficient estimated map to use for the second stage automatic method. In this section, each important parameter will be discussed, followed by a description of how the optimal value was chosen.

First Stage Readout Time

This parameter determines how much of the center of k-space is used to reconstruct the first stage base images. If too much of the data is used, the image phase will have had time to accrue more than ± 1 cycle of phase, thus leading to spurious minima. If too little is used, the base images will not have significant resolution to adequately estimate a field map. Therefore, we should choose the maximum readout time that prevents more than one cycle of phase from accruing. One major issue in doing this is that this parameter depends on what the largest deviation from the expected resonant frequency is across the object.

In most cases where we adequately suppress signal from fat during selective excitation and the magnetic field is properly shimmed, the amount of off-resonance is still significant. A typical well shimmed image at isocenter can have up to around ± 100 Hz off-resonance at 3 T.

Given that 100 Hz is a best case value, we should assume that some images can have much larger maximum off-resonance. Typically ~ 150 Hz at 3 T is a safe assumption. If there is up to 200 Hz of off-resonance, we expect spurious minima to occur at readout times greater than $1/200$ seconds or 5 milliseconds. However, we should also account for additional phase added when we demodulate over a range of frequencies. Thus, if we demodulate over an additional ± 200 Hz, we would expect to see spurious minima occur at readouts longer than $1/400$ seconds or 2.5 milliseconds. If we continue to decrease the maximum allowable readout time, at some point, there is too little data to have sufficient resolution. It is therefore necessary, in some cases, to accept some inaccuracy due to spurious minima in the first stage map.

Through simulation, we can see the effect of varying the amount of readout data used in the first stage field map estimation. Figure 4.3 shows that there are less spurious minima at short readout times, but other errors are introduced. For example, in the first two field maps where only the first 2.3 ms and 3.2 ms of the readout are used, the shape of the phantom is lost especially around edges where the image exhibits high spatial frequency. At long readout times, even though the shape of the map is much clearer and more accurate, spurious minima start to be introduced. This can be seen in the field map shown in Fig. 2 that uses the first 7 ms of the 8 ms readouts. Using that long of a readout introduces spurious minima in both the top right and bottom left part of the phantom. However, it can be seen from these series of maps that the field map is very similar over a fairly wide range of readout times. In this case at 3 T, readout times between 3.2 and 5 milliseconds produce almost identical maps. In this range, we avoid artifacts due to poor resolution and we encounter limited spurious minima. A key note, however, is that this image is an example of where the off-resonance does not vary more than ± 70 Hz. Thus we should not see spurious minima at readout times less than $1/(150+70) = 4.5$ milliseconds, which

is the case in these simulated field maps. Other images might have larger off-resonance, so we should choose our parameter based on a general case and not just this example. In general, 4.1 milliseconds is the preferred first stage readout length at 3T because resolution is sufficient and we have few or no spurious minima.

These simulations are performed at 3 T because off-resonance effects scale proportionally to field strength. Therefore, we expect off-resonance to be less significant at 1.5 T. The recommendation of a 4.1 ms first stage readout is considering maximum tolerable off-resonance. If the absolute off-resonance is much less than that, the first stage readout time can be increased with no penalty. However, since we never know exactly how much off-resonance is present in the image before starting reconstruction, it is best to assume worst case. Increasing τ_1 past the recommended time does not result in a significant gain in field map accuracy even when it is possible to do so without encountering more spurious minima; this effect can also be seen in Fig. 3.3.

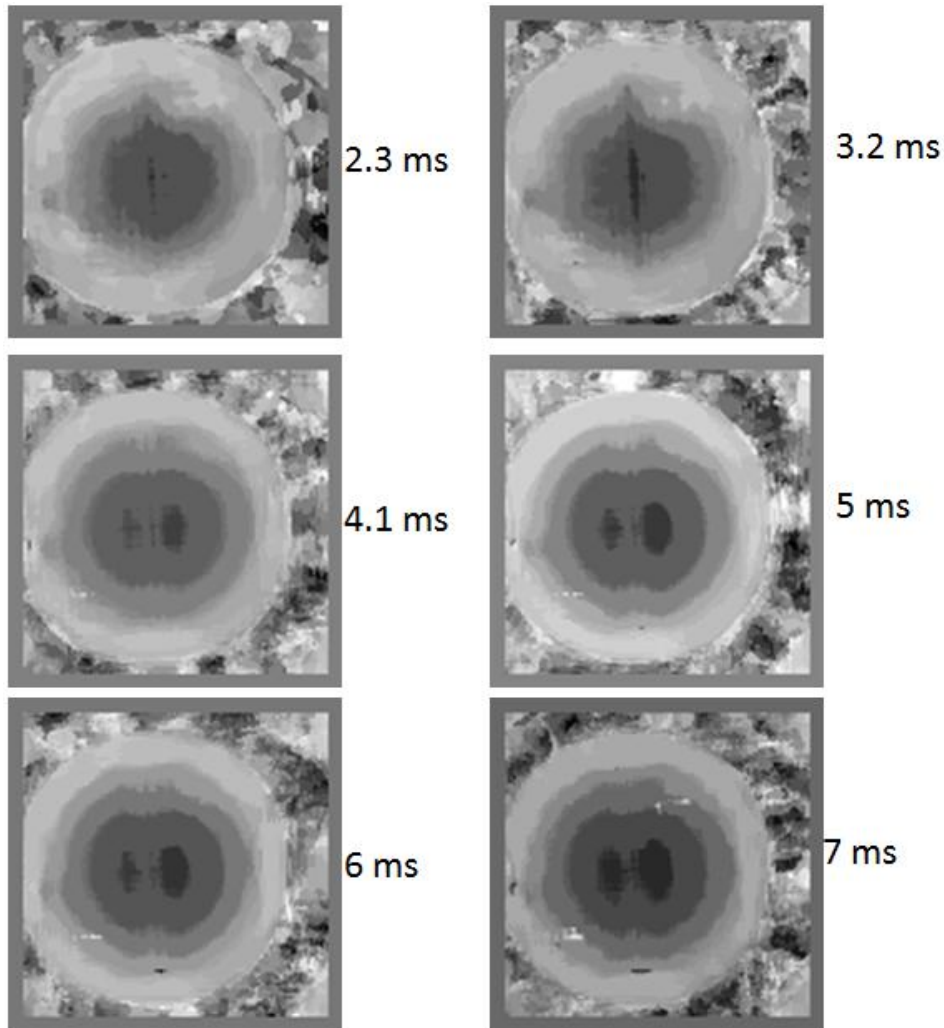


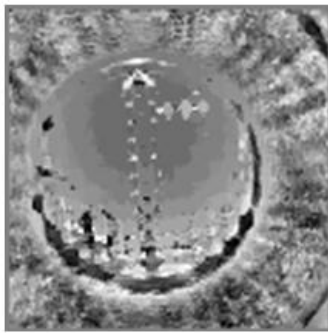
Figure 3.3: First stage low resolution field maps using different amounts of the center of k-space data. The time given next to each image signifies the effective readout time (out of a max of 8 ms) used for the first stage images.

Summation Window Size

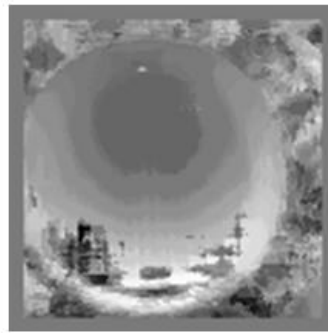
The summation window is the reason that the first stage readout time parameter is robust. Spurious minima are commonly encountered if a small summation window or no summation window is used. However, when the value of the objective function of neighboring pixels is taken into account through local summation, spurious minima are rarely encountered within the area of the object. The summation window is also crucial for avoiding spurious minima where

there are areas of no signal and around edges because if there is no signal from a part of the image, the objective function is always minimized for all demodulation frequencies.

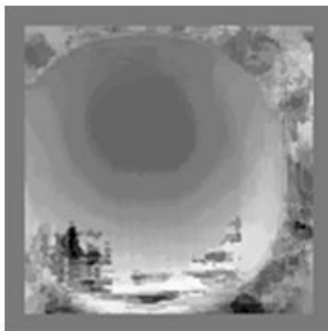
If the summation window is too large, then the map becomes over smoothed and the map loses resolution. However, as with the first stage readout time, this is a robust parameter and the end result is similar over a wide range of summation window sizes. Typically, a good rule of thumb for the summation window is that it should be about 1% of the size of the image. For example, a 512x512 image should have a summation window of 50x50 and a 128x128 image should have a summation window of 12x12. The differences in the field map that results from varying the summation window on the first stage automatic reconstruction of the same image can be seen in Fig. 3.4.



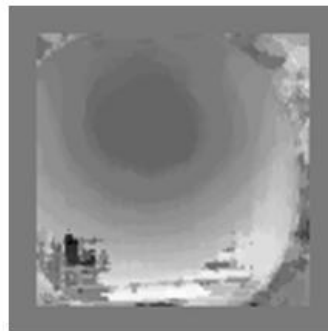
sum win = 4x4



sum win = 12x12



sum win = 16x16



sum win = 22x22

Figure 3.4: Series of field maps from a phantom in an inhomogeneous main magnetic field. Increasing the window size smoothes out the field map and gets rid of many of the spurious minima. The spurious minima that remain are due to the fact that the frequency search range is not large enough to incorporate all of the off-resonant frequencies present in this image (However, increasing the search range would only lead to more spurious minima). NOTE: These field maps are all 128x128 pixels.

Polynomial Fitting and Robust Regression

It can be seen in both Figs. 3.3 and 3.4 that even when much precaution is taken to avoid spurious minima, the map is still noisy and corrupted by quantification due to the fact that we only demodulate at a finite number of off-resonant frequencies. In semiautomatic correction, the first stage acquired map is approximated by a polynomial fit in order to smooth out noise. This approximation assumes that the actual field map varies smoothly in space. It is typical that inhomogeneity is smoothly varying, except at organ boundaries, which are taken care of in the second stage of deblurring. We can use the same approach to apply a polynomial fit in our method to also smooth out both noise and quantification error.

In semiautomatic correction, the polynomial fit is determined by minimizing the L2 norm of a higher order polynomial; typically a fifth order fit is appropriate. The fact that L2 norm regression is sensitive to outliers can become a major problem when spurious minima inevitably appear in a first stage of automatic correction. It is often easy to determine if a point is a spurious minimum because it does not follow the smoothly varying assumption and it appears as a discontinuity in the general off-resonance pattern. That quality makes these points easy to detect. That quality can also be exploited to allow those points to be excluded in determining a polynomial approximation. Normally spurious minima would be the outlying points in ordinary least squares regression, causing the fit to be skewed in areas that contain spurious points. Our

method accounts for this by implementing robust regression that can recognize and suppress outliers from the approximation of the first stage map. This is accomplished through a technique called Iteratively Reweighted Least Squares (IRWLS) (9).

Robust regression techniques involve implementing weighting schemes that give more weight to points that have low residuals and less weight to points with larger residuals. The particular robust regression technique used in our proposed method is IRWLS. The process of IRWLS is outlined below:

1. Fit the first stage field map using ordinary least squares (OLS).
2. Calculate the residuals values for each pixel.
3. Assign weight to each pixel based on a desired weighting function.
4. Perform weighted least squares on the field map using the weight map.
5. Repeat steps 2-4 for a certain number of iterations or until a stop criterion is met.

In step three, we weight each pixel according to its residual value and a weighting function. There are a variety of weighting functions that are typically used for IRWLS fitting that vary in how they assign weight to points with different residual values. A comparison of a few popular weighting functions is shown in Fig. 3.5.

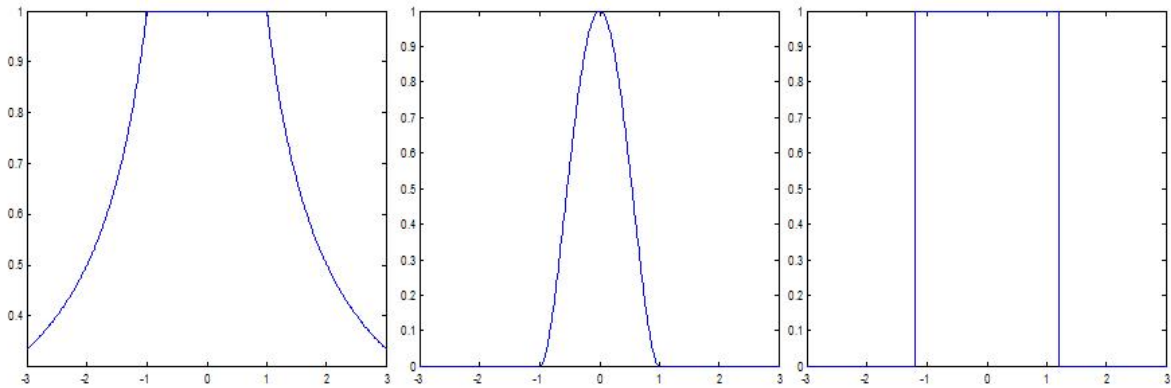


Figure 3.5: Comparison of different IRWLS weighting functions. For all three plots, the x-axis is the tuned residual value and the y-axis is the corresponding weight given to a point with residual x . From left to right: Huber, Bisquare, and Talwar weighting functions with tuning constant, $c = 1$.

In this application, we desire weighting functions that are the strictest about outliers. Restricting outliers is important because it is rare that an outlier would not be a field map inaccuracy. Spurious minima are almost always outliers because they are typically obvious discontinuities in an otherwise smoothly varying field map. This idea is supported through simulation where we found that bisquare and Talwar weighting function gave the best approximation to our simulated maps. When coding this method, we chose to use a Talwar IRWLS weighting function due to its simplicity and complete suppression of large outliers. The results of one simulation is shown in Figs. 3.5 and 3.6.

In simulations on field maps that do not contain such extreme outliers, robust regression generates the same approximation as OLS, ensuring that we do not lose any accuracy under

normal conditions. The only disadvantage of robust regression is the additional computational load.

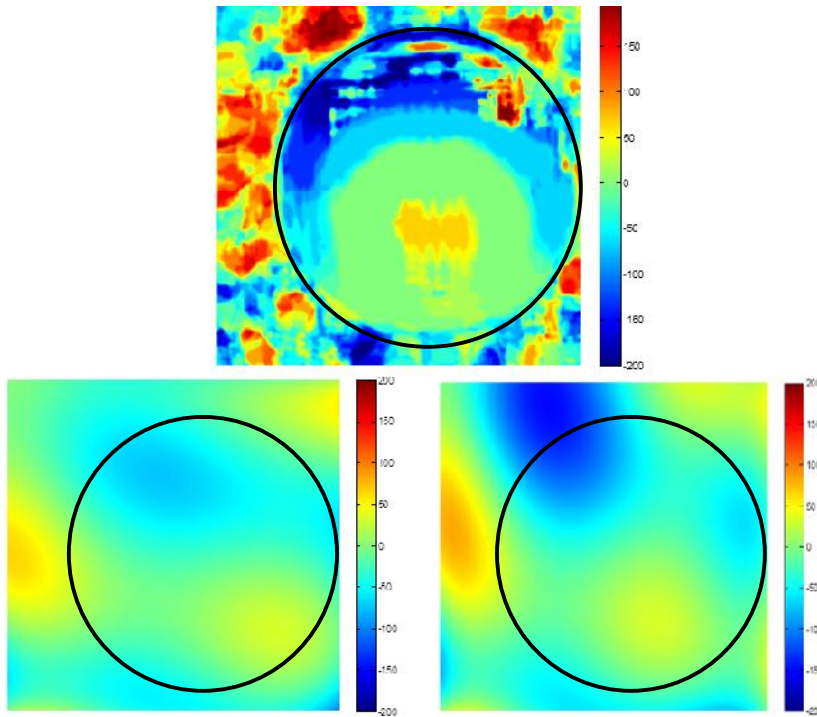


Figure 3.5: Comparison of polynomial fits to the given field map (top). Shows an OLS fit (left) compared to a IRWLS bisquare fit (right). Black circle is shown as an approximate location of the phantom.

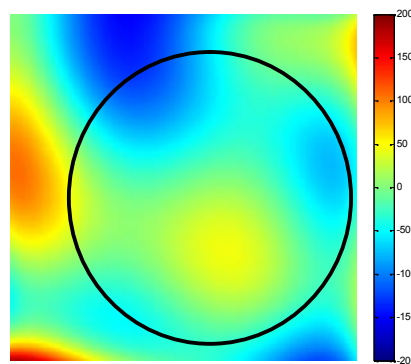


Figure 3.6: Polynomial IRWLS fit using a Talwar weighting function with the tuning constant reduced to 50% of the default value for better outlier suppression. As in Fig. 3.5, the black circle shows approximately where the edges of the phantom are for reference.

Algorithm

1. Generate Chebyshev polynomial coefficients, k-space trajectory, and DCF
2. First Stage Automatic Field Map Generation
 - a. Grid center portion of k-space to use for first stage map generation and very center of k-space for incidental phase images.
 - b. Reconstruct series of base images at different frequencies from the constrained k-space data from part a.
 - c. Remove incidental phase for each image in the series.
 - d. Calculate objective function for each pixel in each base image.
 - e. Calculate the field map that results from choosing the frequency that was used to reconstruct the base image that minimizes the objective function for each pixel.
 - f. Repeat (a-e) for each coil and combine each coil map in a sum-of-squares fashion.
3. Fit the field map using a robust regression scheme, such as IRWLS.
4. Second Stage Automatic Off-Resonance Correction
 - a. Grid full k-space data and very center of k-space for incidental phase images.
 - b. Reconstruct series of base images at different frequency shifts relative to the fitted map from step 2.
 - c. Remove incidental phase for each image in the series.
 - d. Calculate objective function for each pixel in each base image.
 - e. Calculate the field map that results from choosing the frequency that was used to reconstruct the base image that minimizes the objective function for each pixel.
 - f. Repeat (a-e) for each coil and combine each coil map in a sum-of-squares fashion.
5. Reconstruct the final image based on the second stage output field map

Code

Simulations of the two-stage automatic method were first done in Matlab. Weitian Chen's semiautomatic Matlab code was modified to make it fully automatic using the proposed two stage method. After successful implementation in Matlab, the proposed method was implemented in Siemens Image Calculation Environment (ICE) using C++ code. ICE simulates a reconstruction as it would occur on the MRI scanner's computer. Therefore, a reconstruction in ICE will look the same as one performed using that same code on the scanner. The ICE code for this method was written by modifying a semiautomatic ICE program provided by Chris Sica. Even though this code already provided for an automatic first stage, four major changes were necessary to make it work reliably.

1. Changed the way the first stage data is gridded. Because the first stage images are going to be low resolution given that we only reconstruct the center of k-space, the size of the images should reflect that. Given that the base resolution size of the image is 512x512, we can reconstruct the first stage low resolution base images at 128x128 without losing resolution. Smaller image sizes are faster to grid and significantly decrease computational load.
2. Windowed the incidental phase data. We only use the first 1.6 ms of the readout to reconstruct the incidental phase images. Effectively this can be represented as the entire signal equation multiplied by a rectangular window of width 1.6 ms. The multiplication by a rectangular window in the k-domain corresponds to a convolution with a sinc in the spatial domain. The width of the convolved sinc is inversely proportional to the width of the rectangular window. Since the window used to truncate the incidental phase data is small, the image will be convolved with a correspondingly wide sinc function. A better way to truncate the incidental phase data is to multiply it by a Hann window. Convolution with the FFT of

the Hann window results in less distorting effects as convolution with a sinc, therefore leading to a more accurate incidental phase image.

3. Changed the precision of the least squares fit. Originally the code used a function from the Intel Math Kernel Library with single precision. Single precision can accurately represent numbers with up to seven digits. However if we want to fit a 512x512 map using a 5th order polynomial, we have terms in the least squares equation with coefficients that are up to $512^5 = 35184372088832$ which is 14 digits. Smaller maps, for example a 128x128 map, still have terms with coefficients that are $128^5 = 34359738368$, is 11 digits. We lose considerable accuracy using single precision and it was very noticeable in the polynomial maps being output. Changing this to a double precision method solved these errors.
4. Implemented robust regression. IRWLS is used as described preciously in this chapter to effectively suppress outliers in the first stage field map. The implementation used in the reconstructions shown in the results in the next chapter used a Talwar weighting function with a tuning constant chosen such that outliers more than one standard deviation away from the OLS fit were completely suppressed.

Chapter 4

Results

Acquiring Data and Images

The data used to simulate two-stage automatic reconstructions was acquired from the Siemens MAGNETOM Trio 3 T Scanner at the Snyder Building of UVa's Fontaine Research Park. Most of the simulations were performed on phantom images taken using the same cylindrical phantom oriented in the parallel to the length of the bore of the magnet. We chose this water phantom because it contains a grid-like pattern in the axial direction that allows us to more easily assess blurring due off-resonance effects. Our setup also was composed of a four-channel receiver coil that enclosed the phantom.

The parameters for the phantom images were chosen so that the effects of off-resonance would be noticeable. Our reasoning is that we want to prove that this method is robust enough to correctly deblur various sources and amounts of off-resonance. All images are in the axial orientation and were acquired using an 8 interleave spiral sequence with 8.2 ms readouts and a 4 channel receive coil. These images are shown below in Figs. 4.1-4.4. Figure 4.1 can be thought of as a reference image because it has baseline off-resonance effects. The slice in Fig. 4.1 is axial and at isocenter, so there are no concomitant field effects in the image. Also, we assume that under normal conditions, the magnet is well shimmed and the only sources of off-resonance are

intrinsic to the object, such as magnetic susceptibility. Figure 4.1 shows that in a normal imaging slice without the influence of concomitant gradients, significant blurring is still very obvious in an uncorrected image.

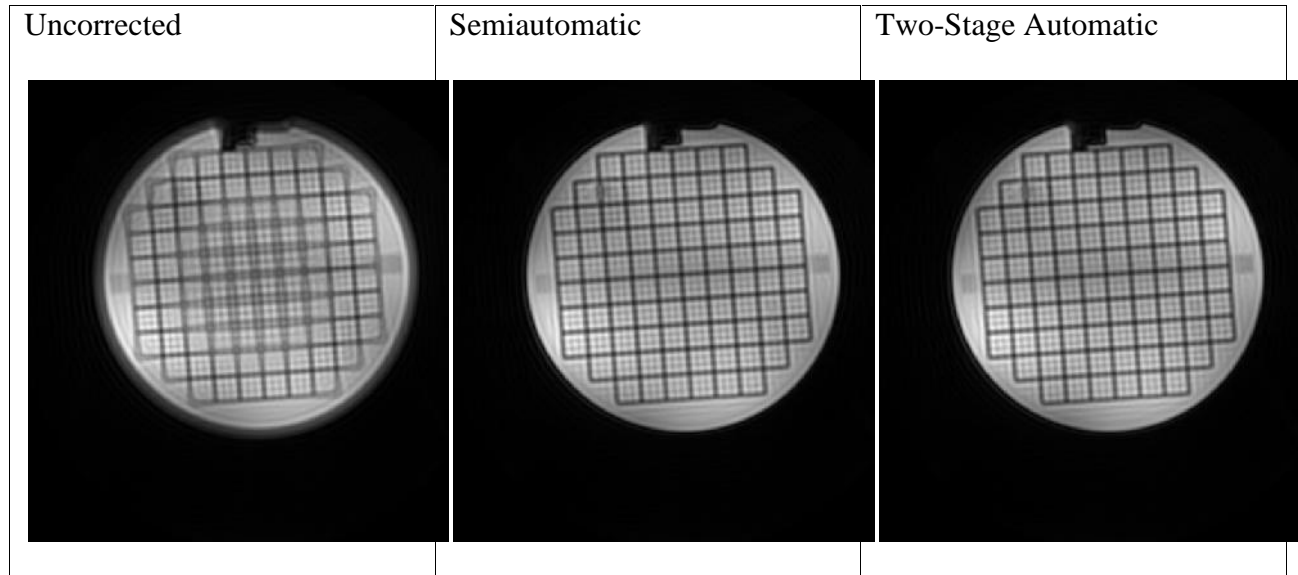


Figure 4.1: Axial slice with a well shimmed field at isocenter

The figure also shows that fully automatic correction works to deblur the image and yields comparable results to a semiautomatic reconstruction. Given the successful reconstruction of Fig. 4.1 using the proposed fully automatic method, we then tested this method's ability to correct other and more significant sources of off-resonance by intentionally varying the shim of the main magnetic field (Fig. 4.2), moving the phantom off isocenter (Fig. 4.3), and introducing fat into the images to simulate chemical shift effects due to fat in the body (Fig. 4.4).

Simulations were also performed on in-vivo spiral myocardial perfusion data, as that is the intended use for this method. In-vivo data was taken from previous spiral myocardial perfusion experiments and reconstructed using the correction methods discussed.

Phantom Results

Automatic off resonance correction can be shown to be just as effective as the semiautomatic method over a wide range of off-resonance effects. Automatic correction can be slightly more challenging due to the fact that one must choose optimal first stage parameters. However, we have shown that the first stage field map can be made to be fairly robust over a wide range of parameters. Also, we use robust techniques to accurately fit a polynomial approximation to a field map even when the field map contains a significant but tolerable amount of artifacts. In Figs. 4.1-4.4, it can be seen that the automatic correction does just as good as the semiautomatic method in terms of deblurring. The difference compared to the uncorrected image is very significant, proving that this method is more desirable than no correction at all.

Further, we can validate the need for using IRWLS fitting in the following set of reconstructions of a phantom in a poorly shimmed magnetic field. In this situation there are areas with a high number of spurious minima in the first stage reconstruction due to phase wrapping. IRWLS is crucial for aiding the fully automatic method in this scenario, particularly in the areas with the greatest level of inhomogeneity. This can be seen in the series of images below. In practice, the magnet will always be shimmed prior to scanning, so this simulation represents an extreme case off-resonance issue and supports the claim that this technique is robust enough to correct the image even in the case of when the first stage encounters many spurious minima. It can be noted that semiautomatic correction works well both with and without IRWLS because the first stage acquired map is not biased by spurious minima. Still, implementing IRWLS for semiautomatic correction does not make the correction any worse; actually it appears to make it better by correcting for slight blurring in the center of the image reconstructed using semiautomatic correction without fitting with IRWLS.

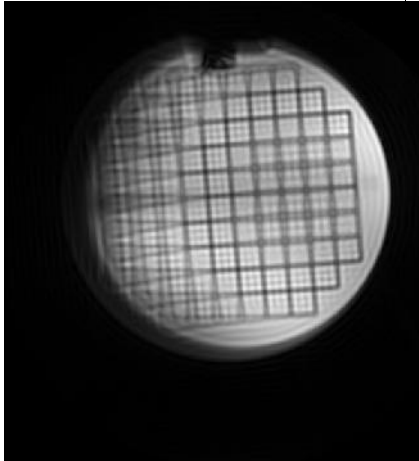
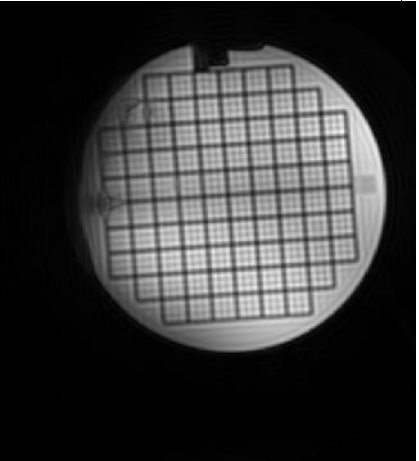
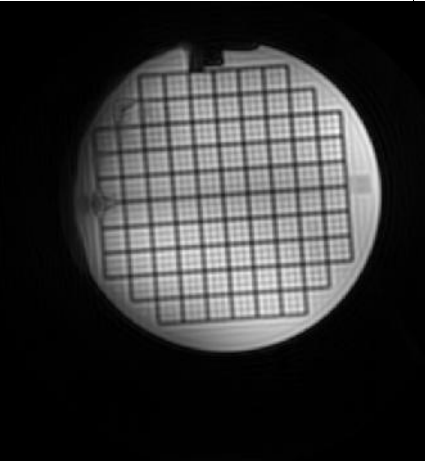
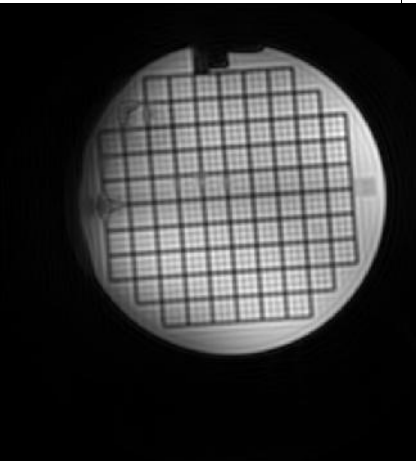
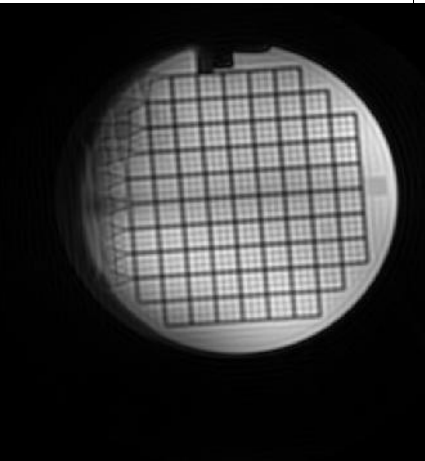
Uncorrected	Semiautomatic w/ IRWLS	Automatic w/ IRWLS
		
	Semiautomatic w/o IRWLS	Automatic w/o IRWLS
		

Figure 4.2: Axial slice with an added linear shim gradient in order to intentionally induce severe inhomogeneity.

Our method uses Chebyshev polynomial coefficients to approximate the exponential term in CP reconstruction. Prior knowledge of the concomitant field is taken into account when calculating those polynomials; thus, our method should correct for concomitant field effects as well as off resonance. We already know from semiautomatic correction (5) that this technique works in lessening blurring caused by concomitant gradients. We can see in our results, shown in Fig. 4.3, that this method similarly corrects for concomitant field blurring. Fully automatic correction accounts for concomitant effects in both the first and second stage field maps.

Semiautomatic correction only considers concomitant phase in the second stage map and assumes it is adequately subtracted out in the first stage map acquisition. Therefore, we can hypothesize that this technique may do better than the semiautomatic technique when it comes to concomitant correction. Our results, particularly Fig. 4.3, suggest this might be true, but it is yet to be proven.

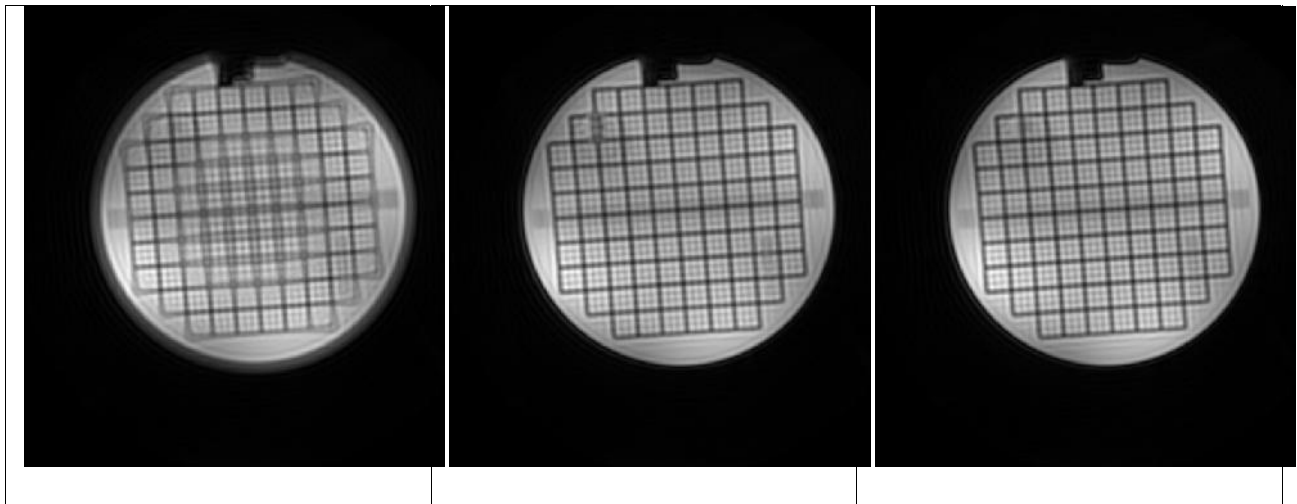


Figure 4.3: Axial slice with a 90 mm offset in Z. From left to right: Uncorrected, Semiautomatic, Automatic.

Adding a cylinder containing oil to the image simulates a highly non-linear field map due to the chemical shift of fat relative to water. Figure 4.4 shows that both semiautomatic and fully automatic correctly deblur the water phantom even when the field off-resonance profile is highly non-linear. Neither method corrects the blurring in the fat phantom because the off-resonant frequency of fat is outside the range of allowable frequencies for both methods. This is acceptable and even desirable because imaging fat is not the goal of our intended application. In fact, fat suppression pulses are almost always applied in-vivo, although it does sometimes show up in images anyway.

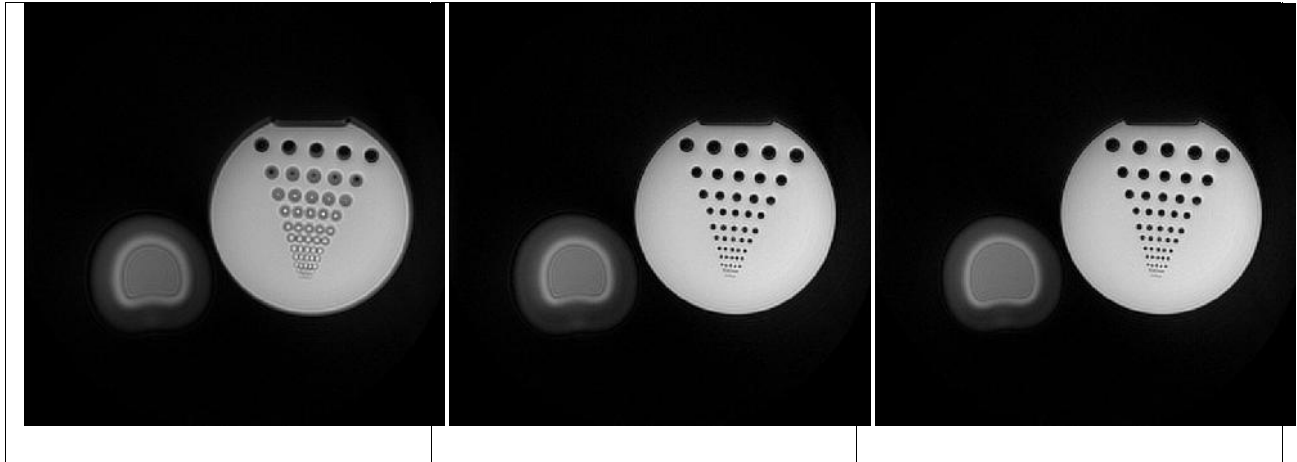


Figure 4.4: Water/Fat Phantom. The fat phantom is the cylinder to the left of the brighter phantom. Both reconstructions correctly deblur the water phantom and ignore the fat phantom. From left to right: Uncorrected, Semiautomatic, Automatic.

In-Vivo Results

Much like the phantom results, automatic correction provides about the same level of deblurring as the semiautomatic method. This is shown in Fig. 4.5, which is one image from a set of myocardial perfusion images over the time course of a stress test. Because this data was acquired at 1.5 T, there is not significant off-resonance which makes it harder to quantify blurring, especially in a single image. Deblurring is more noticeable when looking at all the perfusion in succession. This hopefully proves that this method is ready for use in-vivo, allowing us to stop acquiring field maps for heart perfusion images. The best way to quantify the effectiveness of the automatic method is to compare it to the already adopted semiautomatic method. This can be done using structural similarity and root mean square error analysis (Figs 4.7 and 4.8).

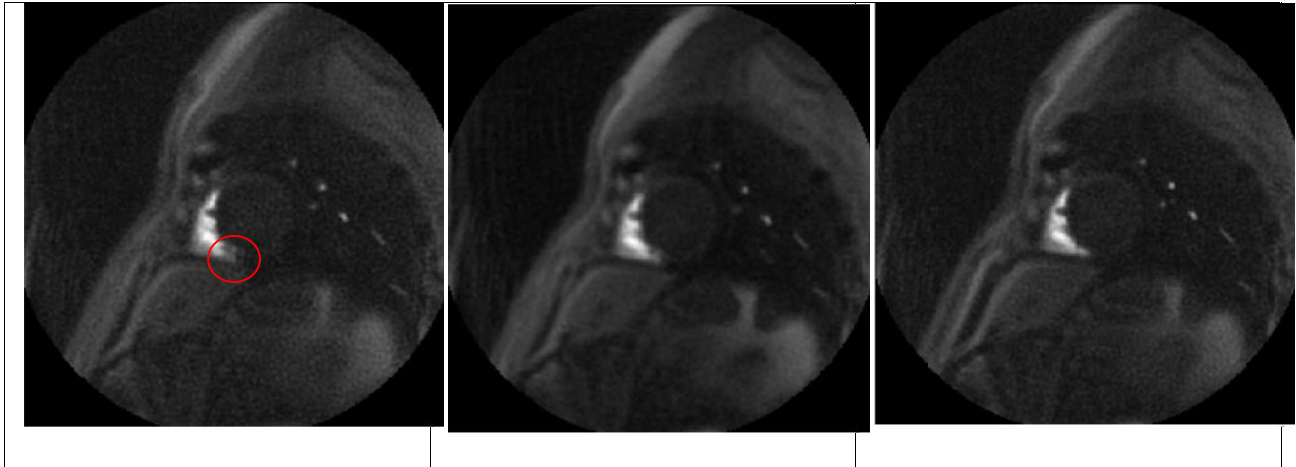


Figure 4.5: Result of correction methods on in-vivo data. The image shown is from a first pass perfusion sequence, right after the contrast enters the right ventricle (a time when it is common to see a lot of blurring). It can be seen that the highlighted blurring in the bottom right of the right ventricle in the uncorrected (left) image gets progressively less-blurry in the semiautomatic (center) and the automatic (right) correction images shown.

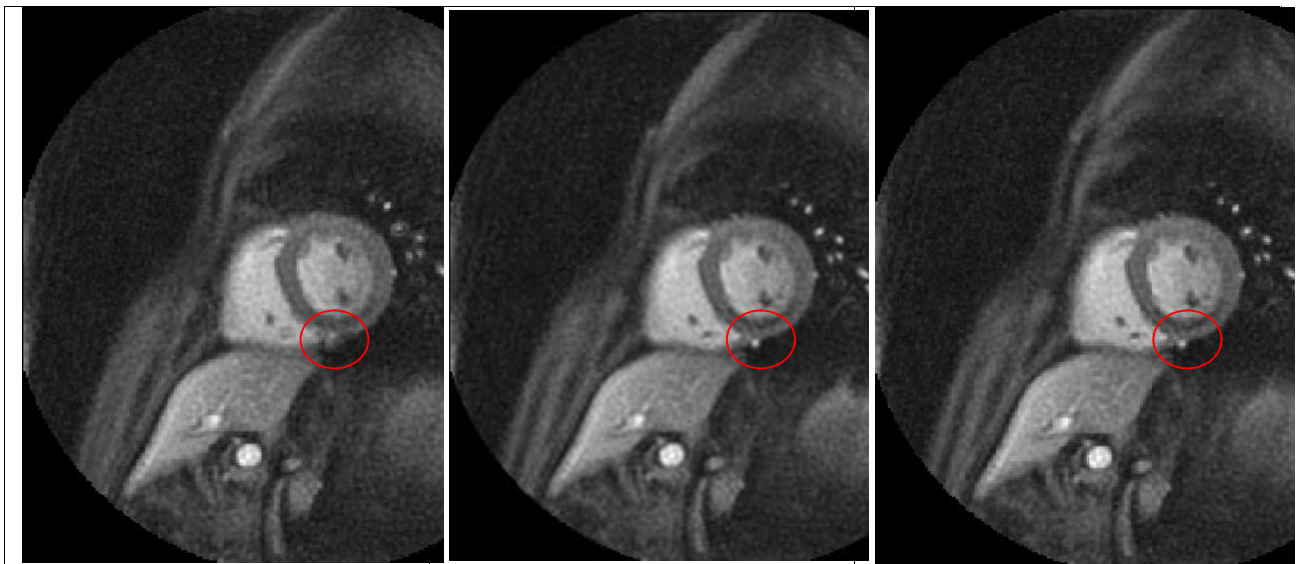


Figure 4.6: Another spiral perfusion reconstruction from a frame at a later time point compared to Fig 4.5. From left to right: Uncorrected, Semiautomatic, Automatic. Using correction fixes the blurring in the highlighted area and makes the highlighted artery visible.

Structural similarity measurements (17) were performed on the spiral perfusion data set to compare the automatic correction to semiautomatic correction. The structural similarity index (SSIM) is a measure of how much two images are similar. SSIM ranges from 0 to 1, with 0 meaning that the two images have no similarity and 1 meaning that they are exactly the same image. SSIM was performed on

all 150 images from the data set. Since it is assumed that semiautomatic correction is the best that can be achieved, the below chart shows the SSIM index of the uncorrected and automatic images compared to the semiautomatic images.

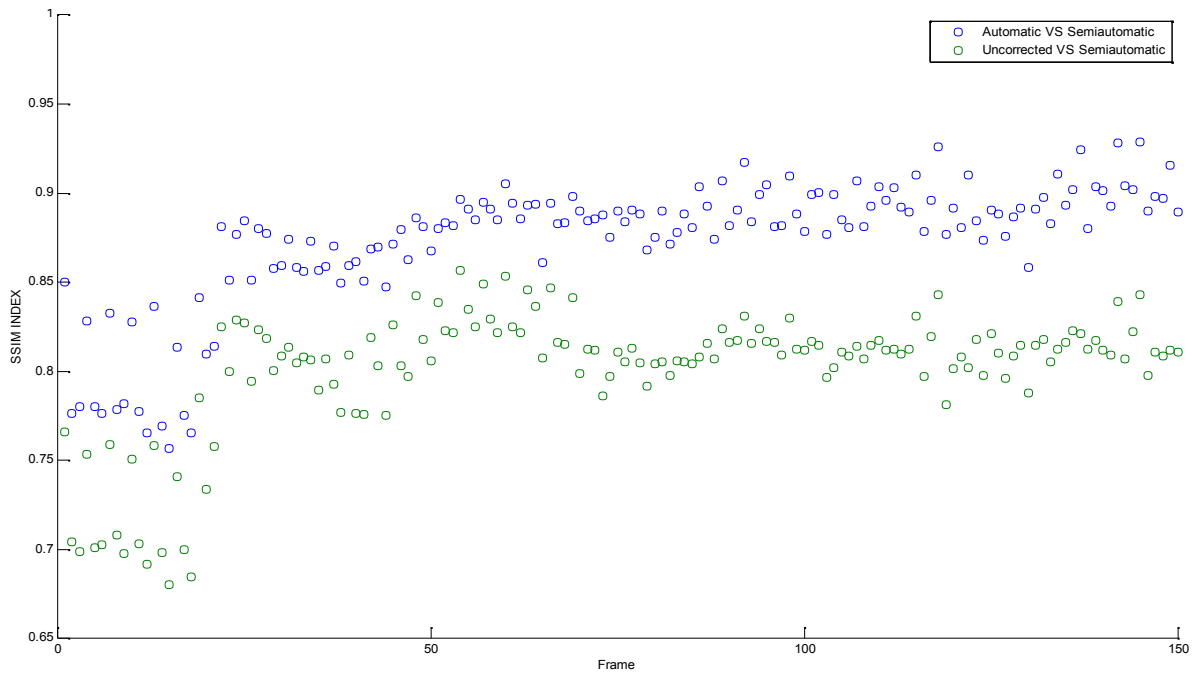


Figure 4.7: Structural similarity index of the automatic correction method compared to the semiautomatic method over 150 spiral myocardial perfusion frames. Also shown is the semiautomatic method compared to uncorrected images as a reference to show that the automatic correction is quantifiably better than using no correction.

A clear trend can be seen that images deblurred with automatic correction are more similar to the semiautomatic correction images than when no correction is used. To prove the validity of the SSIM index, we also include the root mean square error (RMSE) between each automatic and uncorrected image vs the corresponding semiautomatic image, show below. Again we see that the RMSE is smaller for the automatic images, leading to the conclusion that the automatic and semiautomatic reconstructions produce similar images.

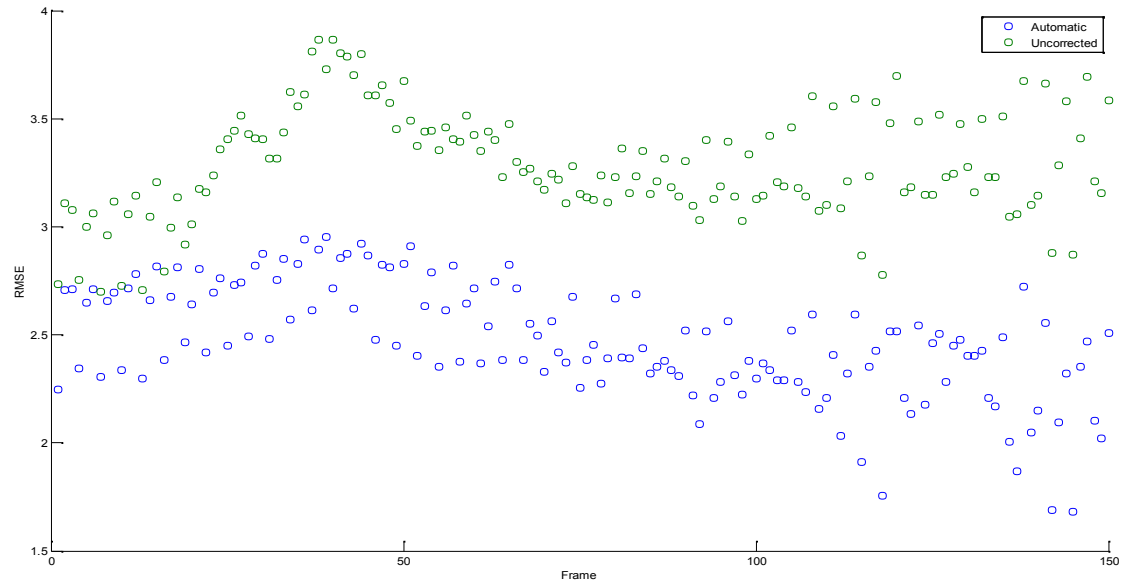


Figure 4.8: Root Mean Square Error (RMSE) of the same 150 images (both using no correction and automatic correction) compared to the semiautomatic corrected images. As in Fig 4.7, it can be seen that the automatic corrected images are noticeably more similar to the semiautomatic images than the uncorrected images.

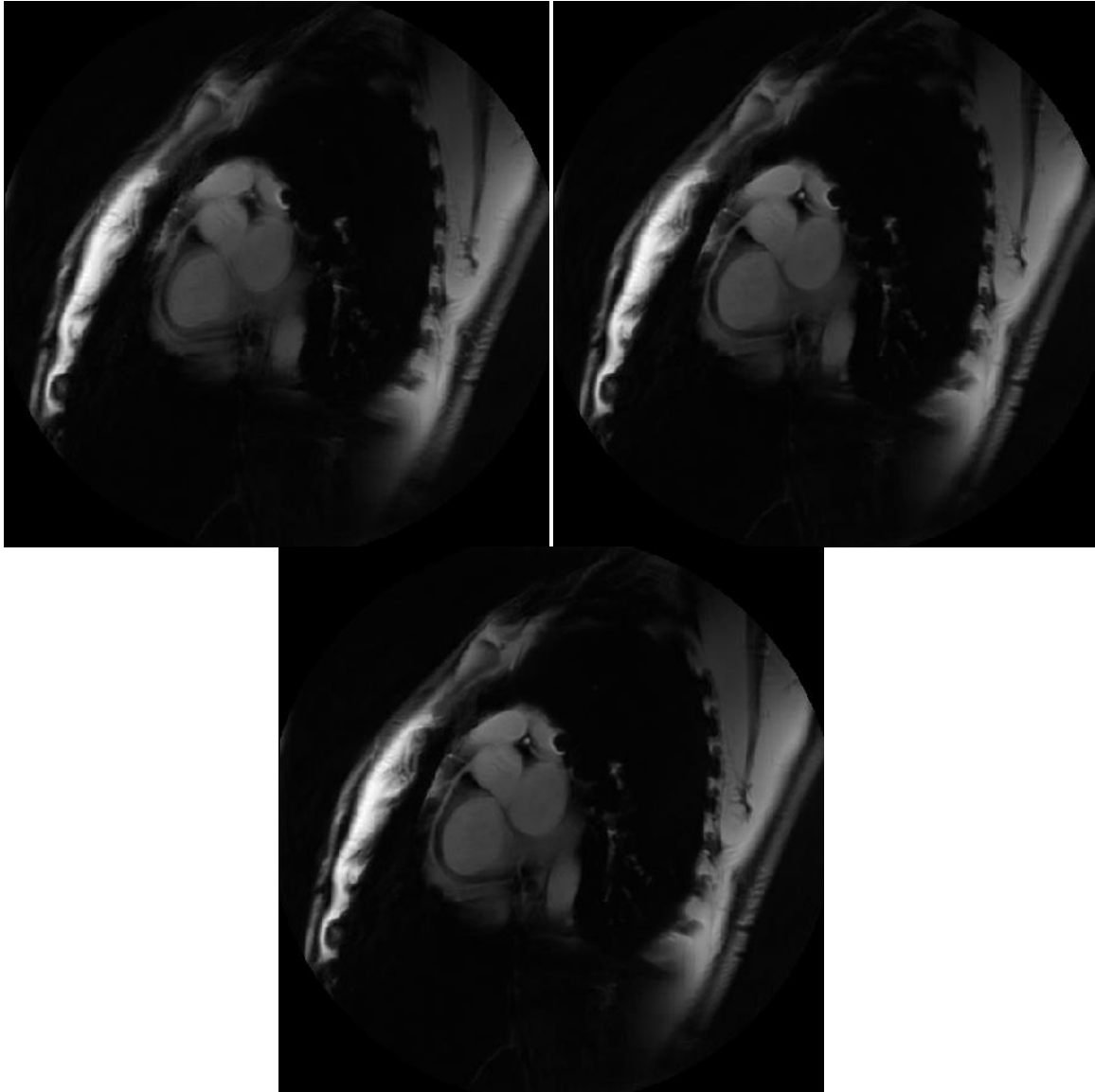


Figure 4.9: A coronary artery image reconstructed using no correction (left), semiautomatic correction (right), and automatic correction (bottom). Both correction schemes significantly reduce blurring and reveal the artery of interest.

We also did SSIM analysis on a different in-vivo data set from a coronary artery imaging sequence (Fig 4.9). Below is a table summarizing the structural similarity of the three images. It is apparent that the semiautomatic and automatic reconstructions produce very similar images (SSIM = .9843), while both images are slightly different from the blurred (uncorrected) image (SSIM \approx .95). The actual images (above) show that this difference is indeed caused by a reduction in blurring.

SSIM	Uncorrected	Semiautomatic	Automatic
Uncorrected	1	.9486	.9473
Semiautomatic	.9486	1	.9843
Automatic	.9473	.9843	1

Computational Efficiency

One drawback is that the automatic method is relatively computationally intensive. For both the automatic and semiautomatic case, the speed will scale with imaging parameters such as size of the image, the number of interleaves, number of imaging slices, and the number of coils used. It should be noted, however, that the computational efficiency of the automatic method is virtually the same as the semiautomatic method in simulation. The following table shows reconstruction times, in minutes, for uncorrected, semiautomatic, and automatic correction. The reconstruction times were done on a laptop PC running the ICE simulation environment. These times would be drastically faster on the scanners reconstruction computer and are only for comparison.

SCAN ID	col	Lines	Channels	Images	Uncorrected	Semiauto	Auto
SP001	3072	8	4	150	4.00	14.22	14.72
SP002	3072	8	4	150	3.92	14.18	15.32
SP003	3072	8	4	150	3.85	14.10	15.10
SP004	3072	8	4	150	3.93	14.10	14.48
SP005	3072	8	4	150	3.90	14.68	14.80
SP006	3072	8	4	150	4.10	14.58	15.43
SP010	3072	8	5	150	5.17	37.67	41.68
SP018	3072	8	9	150	5.12	36.70	41.28
SP007	3072	8	12	150	3.97	16.50	19.25
SP009	3072	8	12	150	6.17	42.87	42.27
SP011	3072	8	12	150	5.38	38.62	40.42
SP012	3072	8	12	150	4.83	34.15	44.20
SP013	3072	8	12	150	4.10	36.23	41.17
SP016	3072	8	12	150	5.28	35.05	40.32
SP017	3072	8	12	150	6.67	26.37	31.20

Chapter 5

Discussion and Conclusion

Discussion

The work presented in this thesis shows that it is possible to simultaneously correct for blurring due to off-resonance and concomitant gradients in spiral images without the extra burden of acquiring a field map. This is accomplished using a two stage, fully automatic method with optimal parameter selection and incorporating a robust polynomial approximation.

The results presented show that this method works at least as well as semiautomatic correction, which is the current gold standard for spiral image deblurring used in our lab. The results shown include a various possible off-resonance scenarios that may occur during a scan to prove the robustness of the fully automatic method. The semiautomatic method is still preferred when we can acquire a field map with no penalty due to its superior robustness and computational efficiency.

This work is particularly important to time limited MRI scans where it is undesirable to prolong scan time by acquiring a field map for use in semiautomatic correction. This method is expected to increase the diagnostic ability of perfusion related imaging sequences, such as myocardial stress perfusion MRI and arterial spin labeling (ASL) MRI.

Recommendations for Future Work

The improved two stage automatic correction method outlined in this thesis is currently implemented in Siemen's ICE simulation environment. The next step is to load this reconstruction onto the scanner so that it can be used directly in conjunction with a patient scan.

Although modifications to the spiral sequences were discussed, they were not implemented as part of this research. A next step would be to modify a spiral sequence that currently acquires a field map, such as the spiral myocardial perfusion sequence, so that it no longer acquires a field map. It would then be possible to adjust the sequence to acquire more useful imaging data, such as collecting more slices or better SNR.

The major drawback of the fully automatic method is computational efficiency. Ideally, off-resonance correction would be implemented in real time imaging. This would require that the reconstruction time be negligible, which is currently not the case. Although, the Chebyshev approximation significantly reduces the computational load, it is not fast enough. The best hope for speeding up reconstruction time is the advancement in computing. Multi-core processors that allow threading are significantly reducing reconstruction time. Also it is likely that recent advances in GPU computing will further reduce computation time.

This method supplements the push for researchers to develop accelerated imaging methods. Work on compressed sensing (CS) is allowing for images to be reconstructed with full resolution and FOV while acquiring significantly fewer lines of k-space. How or if this method can be applied to spiral imaging is yet to be seen. Parallel imaging is another technique that is currently being used to accelerate scan time. Semiautomatic off-resonance correction has already been used to aid parallel reconstructions in spiral images. It is likely that the automatic correction method will produce similar results, adding to the acceleration factor of parallel imaging.

Conclusion

The method created is an optimized automatic off-resonance and concomitant gradient correction algorithm which can be used in place of semiautomatic correction for applications which it is desirable to not acquire a field map. The validity of this method has been shown through both phantom and in-vivo reconstructions with very positive results. The semiautomatic method is still preferred when we can acquire a field map with no penalty due to its robustness and computational efficiency.

Chapter 6

Bibliography

- (1) CH Meyer, B Hu, DG Nishimura, and A Macovski, “Fast Spiral Coronary Artery Imaging,” *Magn Reson Med*, vol. 28, no. 2, pp. 202–213, Dec 1992.
- (2) DC Noll, JM Pauly, CH Meyer, DG Nishimura, and A Macovski, “Deblurring for Non-2DFT MRI,” *Magn Reson Med*, vol. 25, no. 2, pp. 319–333, Jun 1992.
- (3) KF King, A Ganin, XJ Zhou, and MA Bernstein, “Concomitant gradient field effects in spiral scans,” *Magnetic Resonance in Medicine*, vol. 41, no. 1, pp. 103–112, 1999.
- (4) Schneider E, Glover G. Rapid in vivo proton shimming. *Magn Reson Med* 1991;18(2):335–47.
- (5) Chen W, Meyer CH. Semiautomatic off-resonance correction in spiral imaging. *Magn Reson Med* 2008; **59**: 1212–1219.
- (6) Chen W, Sica CT, Meyer CH. Fast conjugate phase image reconstruction based on a Chebyshev approximation to correct for B0 field inhomogeneity and concomitant gradients. *Magn Reson Med* 2008; **60**: 1104–1111.

- (7) Man LC, Pauly JM, Macovski A. Improved automatic off-resonance correction without a field map in spiral imaging. *Magn Reson Med* 1997;37:906–913.
- (8) Lee D, Nayak KS, Pauly JM. Reducing spurious minima in automatic off-resonance correction for spiral imaging. In: *Proceedings of the International Society of Magnetic Resonance in Medicine*, Kyoto, Japan. 2004. p. 2678.
- (9) Andersen, Robert, ed., *Modern Methods for Robust Regression*. Thousand Oaks: SAGE Publications, Inc., 2008.
- (10) Irarrazabal P, Meyer CH, Nishimura DG, Macovski A. Inhomogeneity correction using an estimated linear field map. *Magn Reson Med* 1996;35(2):278–82.
- (11) Chen W, Meyer CH. Fast automatic linear off-resonance correction method for spiral imaging. *Magn Reson Med* 2006; **56**: 457–462.
- (12) D. C. Noll, J. A. Fessler, and B. P. Sutton, “Conjugate phase MRI reconstruction with spatially variant sample density correction,” *IEEE Trans. Med. Imag.*, vol. 24, no. 3, pp. 325–336, Mar. 2005.
- (13) Man LC, Pauly JM, Macovski A. Multifrequency interpolation for fast off-resonance correction. *Magn Reson Med* 1997; **37**: 785–792.

- (14) WH Press, SA Teukolsky, WT Vetterling, and BP Flannery, Numerical recipes in C, Cambridge University Press Cambridge, 1992.
- (15) D. C. Noll, C. H. Meyer, J.M. Pauly, D. G. Nishimura, and A. Macovski, "A homogeneity correction method for magnetic resonance imaging with time-varying gradients," *IEEE Trans. Med. Imag.*, vol. 10, no. 4, pp. 629–637, Dec. 1991.
- (16) Salerno M, Sica CT, Kramer CM, Meyer CH. Optimization of spiral-based pulse sequences for first-pass myocardial perfusion imaging. *Magn Reson Med* 2011; **65**: 1602–1610.
- (17) Z. Wang, A. C. Bovik, H. R. Sheikh, and E. P. Simoncelli, "Image quality assessment: From error measurement to structural similarity" *IEEE Transactions on Image Processing*, vol. 13, no. 1, Jan. 2004.